Full Picture of Lattice Deformation in a $Ge_{1-x}Sn_x$ Micro-Disk by 5D X-ray Diffraction Microscopy

Cedric Corley-Wiciak Marvin H. Zoellner Agnieszka A. Corley-Wiciak Fabrizio Rovaris Edoardo Zatterin Ignatii Zaitsev Gianfranco Sfuncia Giuseppe Nicotra Davide Spirito Nils von den Driesch Costanza L. Manganelli Anna Marzegalli Tobias U. Schulli Dan Buca Francesco Montalenti Giovanni Capellini Carsten Richter*

Dr. C. Corley-Wiciak, Dr. E. Zatterin, Dr. T. Schulli
European Synchrotron Radiation Facility, 71 avenue des Martyrs, CS 40220, 38043 Grenoble Cedex 9, France
Dr. C. Corley-Wiciak, Dr. M. H. Zoellner, A. A. Corley-Wiciak, I. Zaitsev, Dr. D. Spirito, Dr. C. L. Manganelli, Prof. G. Capellini
Leibniz-Institut für innovative Mikroelektronik, Im Technologiepark 25, 15236 Frankfurt(Oder), Germany
Email Address: capellini@ihp-microelectronics.com
A. A. Corley-Wiciak
RWTH Aachen, Aachen, Germany
Dr. F. Rovaris, Prof. A. Marzegalli, Prof. F. Montalenti
L-NESS and Department of Materials Science, University of Milano-Bicocca, Via Roberto Cozzi 55, 20125 Milano, Italy
Dr. G. Sfuncia, Dr. G. Nicotra
CNR-IMM, Zona Industriale Strada VIII, 5, Catania 95121, Italy
Dr. N. von den Driesch, Dr. D. Buca
Peter Grünberg Institute 9 (PGI 9) and JARA-Fundamentals of Future Information Technologies, Forschungszentrum Jülich, Jülich, 52425, Germany
Prof. G. Capellini
Dipartimento di Scienze, Universita Roma Tre, Roma 00146, Italy
Dr. C. Richter
IKZ – Leibniz -Institut für Kristallzüchtung, Max-Born-Straße 2, 12489 Berlin, Germany

Keywords: *X-ray nanoprobe, Lattice Strain, GeSn, 3D microstructures*

Lattice strain in crystals can be exploited to effectively tune their physical properties. In microscopic structures, experimental access to the full strain tensor with spatial resolution at the (sub-)micrometer scale is at the same time very interesting and challenging. In this work, we show how scanning X-ray diffraction microscopy, an emerging model-free method based on synchrotron radiation, can shed light on the complex, anisotropic deformation landscape within three-dimensional microstructures. This technique allows the reconstruction of all lattice parameters within any type of crystal with submicron spatial resolution and requires no sample preparation. Consequently, the local state of deformation can be fully quantified. Exploiting this capability, we have mapped all components of the strain tensor in a suspended, strained $Ge_{1-x}Sn_x$ /Ge microdisk. We were able to unambiguously correlate subtle elastic deformations with structural defects, three-dimensional microstructure geometry, and chemical variations, as verified by comparison with complementary electron microscopy and finite element simulations. The methodology described here is applicable to a wide range of fields, from bioengineering to metallurgy and semiconductor research.

1 Introduction

The variation of physical properties in a crystal due to local or global deviations from its ideal lattice is a key aspect of materials science, as it provides the opportunity to tailor the material properties for a specific purpose. This possibility is exploited in a variety of fields, including micro- and optoelectronics [1], plasmonics [2], electrochemistry [3], solar cell design [4], thermoelectrics [5], catalysis [6], bioengineering [7], and quantum technology [8]. The physical quantity describing local perturbations of the idealized periodic arrangement of atoms in a real crystal is called lattice strain.

Although strain is generally described by a symmetric rank two tensor, most discussions in the literature focus on scalar projections or a few components [9, 10]. The shear strain, on the other hand, is often neglected or difficult to quantify. In fact, any local perturbation of a crystal lattice leads to a general form of the strain tensor due to the elastic interaction with its environment and the mediation of stress. The propagation of stress and strain in a three-dimensional (3D) medium is often particularly complex and counterintuitive [11, 12].

A non-destructive measurement of all components of strain and its relaxation in 3D is not commonly available, but is usually inferred from finite element modeling (FEM) [13]. One reason for this is that the most widely used strain probes do not penetrate the material sufficiently to study deeper layers, or rely on cutting out specific regions [14, 15]. Gaining direct, model-free access to the spatial distribution of all strain components becomes particularly important in patterned 3D micro- and nanostructures, which are typically subjected to inhomogeneous mechanical stress [16]. This points to the need for more advanced techniques that combine high lattice sensitivity with nanoscale resolution. The synchrotron-based method used in this work, scanning X-ray diffraction microscopy (SXDM), provides unique sensitivity and accuracy to strain and allows model-free mapping of all components of deformation with submicron resolution [17, 18].

An exemplary case where lattice strain directly impacts the physics behind widespread applications is in the realm of information and computation technologies. Indeed, our ever-evolving world and society require the development of devices with entirely new functionalities, low cost, ease of integration, and energy efficiency. The continuous improvement of the silicon-based microelectronics platform, thanks to its scalability, low-cost and high-yield manufacturing, has enabled it to keep pace with the required performance increases [19, 20]. However, this workhorse of information technology cannot by itself provide all the properties required for multipurpose functionalities, as has already been demonstrated in the case of silicon photonics, where germanium had to be added to the technology to perform different tasks [21]. Similarly, in the best case, the next generation of materials will come from the group IV periodic table, with the possibility of heteroepitaxial growth on Si and with properties that could enable new functionalities for innovative applications, following the so-called "more-than-more" path [22]. Ideally, they should offer significant improvements in band structure engineering and be abundant in nature and environmentally friendly.

All of these characteristics are exemplified by a new system of materials: The tin-based group IV alloys $Ge_{1-x}Sn_x$ and $Si_yGe_{1-x-y}Sn_x$. The optical and electronic properties of this binary/ternary alloy can be tuned to a large extent by controlling the stoichiometry and/or the lattice strain. In particular, the latter is a powerful tool to change the fundamental band gap from non-direct to direct, with huge improvements in the optical properties, leading to the demonstration of a room temperature optically pumped laser [23] and an electrically pumped laser [24] based on $Ge_{1-x}Sn_x$.

Using this material system as an example, we show how the SXDM technique can be used to study complex lattice deformation landscapes in 3D micrometric structures. In particular, we obtain the spatial distribution of the strain tensor in a lithographically defined microdisk made of a partially plastically relaxed $Ge_{1-x}Sn_x$/Ge epitaxial heterostructure [10].

Thus, we demonstrate that SXDM measurements provide an unprecedented level of quantification of local lattice inhomogeneities in patterned 3D microstructures, covering elastic deformation due to geometric shaping, strain fields emanating from dislocations, alloy content fluctuations and their associated strain fields. In addition, we review the validity of the assumptions required to determine stoichiometric fluctuations in alloys from diffraction data and their effect on the crystal lattice. The experimental results are corroborated by dedicated FEM simulations, demonstrating how SXDM can lay a foundation for the development of realistic micromechanical models.

2 Results and Discussion

2.1 Scanning X-ray Diffraction Microscopy

SXDM measurements were performed on the microdisk shown in **Figure 1a**, yielding two-dimensional spatial maps of the scattered X-ray intensity resolved in 3D reciprocal space near a certain Bragg reflection, as illustrated in **Figure 1b**. Thus, two direct and three reciprocal spatial dimensions are probed, yielding a five-dimensional (5D) dataset. Then, maps of all components of lattice strain and rotation tensors are calculated, as described in the Experimental Section, from a set of such 5D datasets for three asymmetric Bragg reflections.

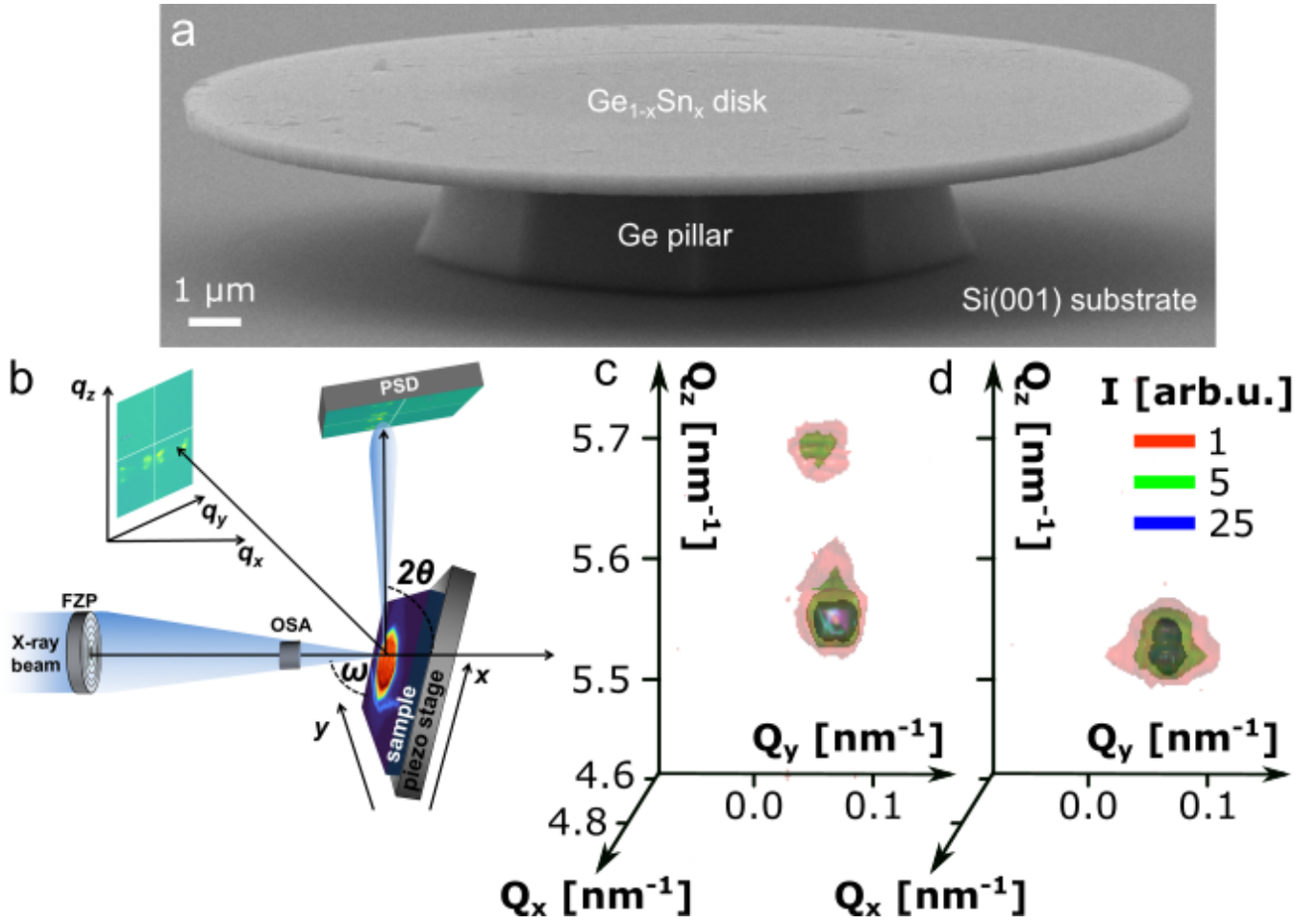

Figure 1: Geometry of the sample, experimental setup and reciprocal space maps. (a) SEM image of a $Ge_{1-x}Sn_x$ microdisk in side view. (b) Schematic of the SXDM setup at ID01/ESRF. (c) 3D RSM in cartesian l coordinates of the 335 Bragg reflection above the pillar. (d) 3D RSM on the free-standing rim.

An exemplary 3D reciprocal space map (RSM) of the 335 Bragg reflection is presented in **Figure 1c**, measured on the center point of the microdisk, where intense Bragg peaks from the Ge virtual substrate and the $Ge_{1-x}Sn_x$ active layer are observed. In **Figure 1d**, we show the corresponding 335 RSM acquired on the outer region of the microdisk, where the Ge virtual substrate has been etched away, leaving the free-standing $Ge_{1-x}Sn_x$ to undergo elastic relaxation. In this area, the intense Bragg peak from the $Ge_{1-x}Sn_x$ is present together with a much weaker signal from a Ge film. The latter diffuse signal is attributed to residual Ge remaining either on the surface of the Si substrate or the bottom of the microdisk.
The two signals are well separated in reciprocal space due to the larger volume of the $Ge_{1-x}Sn_x$ unit cell compared to pure Ge. This is one of the key features of the technique: the analysis of separate reciprocal lattice points enables to map separately the lattice of different layers of a heterostructure, thus giving a "quasi-tomographic" description of the sample. In this case, it allows to study the deformation in the Ge and $Ge_{1-x}Sn_x$ layer individually.

2.2 Maps of Lattice Strain and Rotation

First, we demonstrate that a comparison between the synchrotron experiment and our FEM simulations allows for thorough comprehension of the lattice deformation involved in elastic relaxation. In **Figure 2**, experimental SXDM maps for the microdisk of ≈ 420 nm thickness and an average Sn content of $x_{Sn} \approx 11.8$ % are juxtaposed with FEM simulations obtained using *Comsol Multiphysics*, as described in the Experimental Section. The maps were extracted as 2D projections of the 3D model by the depth average through the thickness of the $Ge_{1-x}Sn_x$ layer. SXDM maps for the plastically relaxed Ge layer are provided in the supplementary information (SI).
As expected based on the heteroepitaxial lattice mismatch, the region of the $Ge_{1-x}Sn_x$ layer connected to the Ge pillar is compressively strained along the in-plane directions. Therefore, at the center of the pillar (within the green circle) the average in-plane elastic strain $\varepsilon_{\parallel} = \frac{1}{2}\left(\varepsilon_{xx} + \varepsilon_{yy}\right)$ amounts to $\varepsilon_{\parallel} \approx -0.50\%$. Counteracting this in-plane distortion, the lattice exhibits a positive out-of-plane strain $\varepsilon_{zz} \approx +0.35$ % in line with the Poisson effect. From the experimental strains, we calculate the average in-plane stress in the center region of the $Ge_{1-x}Sn_x$ from Hooke's law as $\sigma_{xx} \approx \sigma_{yy} \approx -500$ MPa, of a typical magnitude found in strained epitaxial thin films [25]. The outer section of the microdisk, where the Ge support has been etched away, is free to relax to release the elastic energy stored in the $Ge_{1-x}Sn_x$ layer. Thus, on the rim of the microdisk i.e. in the area between the green and red circles, the symmetric strains ε_{xx}, ε_{yy}, ε_{zz} are reduced in magnitude and approach zero (panels **a-f**). This observation is quantitatively confirmed by Raman μ-spectroscopy as an independent, more coarsely spatially resolved technique for strain mapping (see Supplementary Figure 8).
In general we observe a striking agreement, both qualitative and quantitative, of experimental data and simulation concerning the overall strain distribution. The main discrepancy are semi-periodic modulations seen as vertical and horizontal lines with typical spatial distance of 1 μm, which are visible in the experimental maps of all components of strain and referred to as "cross hatch pattern" (CHP). These lines are a trace of misfit dislocations (MDs) that are a result of plastic relaxation and aligned in crystallographic $< 110 >$ directions, since these are the intersections of the $\{111\}$ glide planes with the surface [26].
As seen in the experimental data, not the whole area of the microdisk, indicated by the dashed red circles in **Figure 2**, could be reconstructed. This is due to a strong lattice bending of the outer parts and a limited detection range of the measurement setup. Nevertheless, based on the four-fold crystallographic symmetry of the system, the data contains all information needed for the comparison with theory. The FEM model relies on cylindrical symmetry and accounts for the spatial average of the plastic relaxation extracted from X-ray diffraction (XRD) measurements. Moreover, a non-homogenous spatial 3D profile of the Sn content in the $Ge_{1-x}Sn_x$ alloy [26], and deviations of elastic parameters in the epitaxial layers from the literature values [27] for bulk material, may contribute to small local mismatch between experiment and theory. The dislocation-driven strain fields and the associated fluctuations of stoichiometry are discussed in the next subsections.
The transition region between the pillar and the under-etched part of the microdisk exhibits the strongest local changes of strain, which also include significant out-of-plane shear strain, ε_{xz} and ε_{yz}, that is reproduced both in the measurement and the simulation (panel **g** vs **j** and **h** vs **k**). An illustrative explanation is that, while the bottom part of the microdisk is connected to the pillar, its upper part is rather free to relax laterally, leading to shear stress and therefore to both the curvature and the mentioned shear strains. For the same reason, in the maps of the in-plane shear strain (panels **i, l**), we observe a quadrupole whose lobes are oriented diagonally within the *xy* plane. Moreover, line-shaped fluctuations of the three shear strains are observed in the center area of the experimental maps due to the MD network.

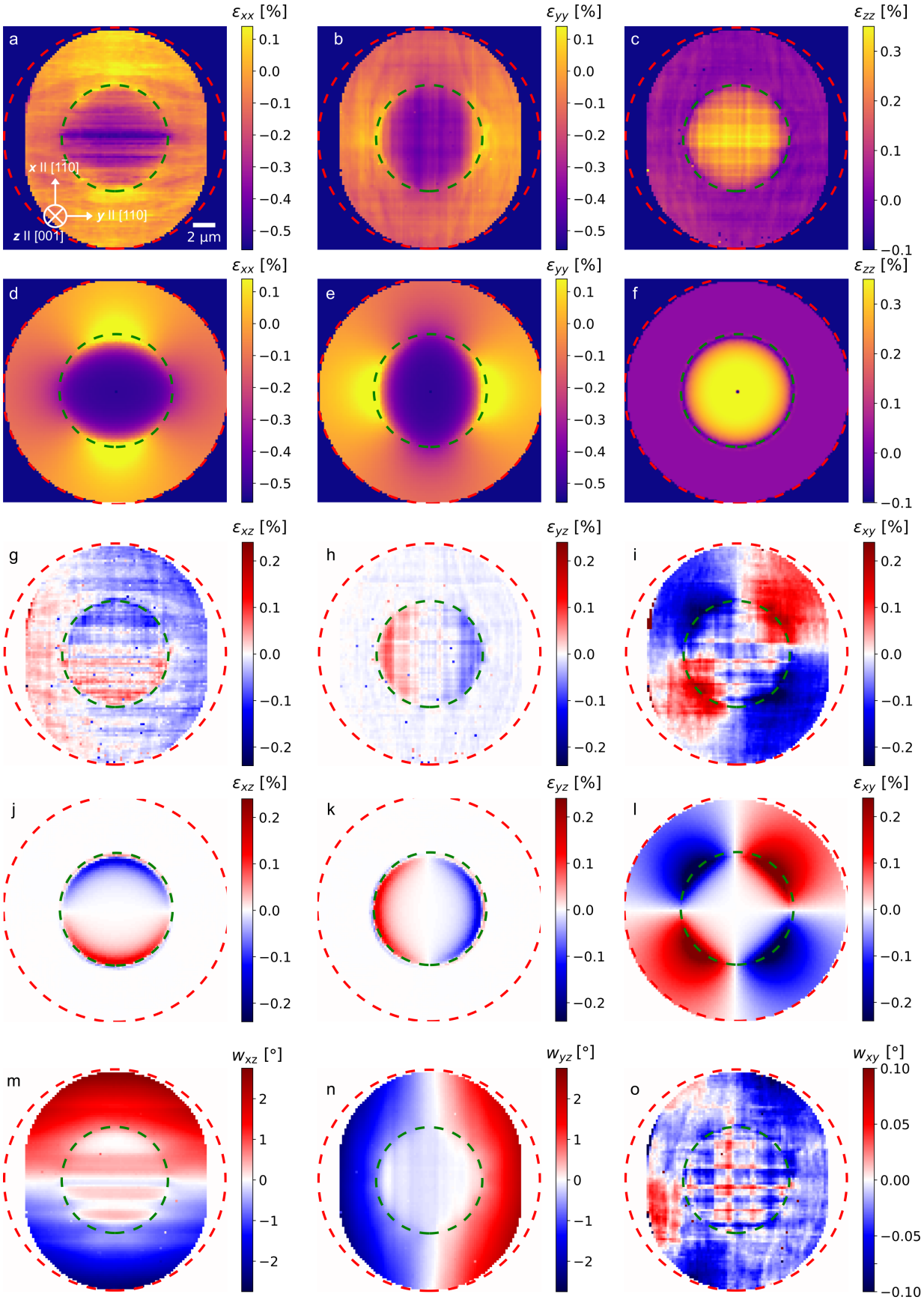

Figure 2: Maps of lattice strain and rotation in the $Ge_{1-x}Sn_x$ microdisk. Experimental SXDM maps of normal strains (a) ε_{xx} (b) ε_{yy} (c) ε_{zz}. The inset arrows indicate the directions of the lattice planes. Simulated FEM maps of (d) ε_{xx} (e) ε_{yy} (f) ε_{zz}, SXDM shear strain maps of (g) ε_{xz} (h) ε_{yz} (i) ε_{xy}, FEM maps of (j) ε_{xz} (k) ε_{yz} (l) ε_{xy}, SXDM maps of lattice rotations (m) w_{xz} (n) w_{yz} (o) w_{xy}. The dashed green and red circles respectively indicate the extent of the supporting Ge pillar and suspended $Ge_{1-x}Sn_x$ microdisk.

The components of the lattice rotation tensor $\underline{\mathbf{w}}$ in the $Ge_{1-x}Sn_x$ are presented in **Figure 2m-o**. The spatial distribution of the lattice rotations w_{xz} (pitch) and w_{yz} (roll) are dominated by the tilt of the lattice planes corresponding to the convex (hill-like) curvature of the microdisk, which is caused by the deformation and elastic relaxation of the microdisk due to the compressive stress applied at the bottom of the $Ge_{1-x}Sn_x$ layer along the in-plane directions. The central part of the microdisk supported by the pillar, within the dashed green circle, is flat and oriented parallel to the substrate surface. Meanwhile, shear stress in the transition part and a trend towards higher Sn content close to the surface drive an overall convex curvature of the free-standing rim.

2.3 Dislocation-induced Strain Modulation

The horizontal and vertical lines in the strain maps are a consequence of plastic relaxation via dislocation injection, alleviating the lattice mismatch in heteroepitaxial growth, as in the present case for $Ge_{1-x}Sn_x$ on a Ge virtual substrate. It is well established in heteroepitaxy that, beyond a certain critical layer thickness, the elastic strain energy due to the lattice mismatch exceeds the energy needed to form MDs at the heterointerface. At this stage, plastic relaxation sets in and reduces the heteroepitaxial strain [28]. The predominant plastic relaxation mechanism in $Ge_{1-x}Sn_x$ is the nucleation of dislocation loops, whose subsequent glide results in running threading dislocation arms and the deposition of 60° MD segments aligned to the crystallographic $\langle 110 \rangle$ directions [29], forming a complex MD network at the heterointerface.
We point out here that also the Ge virtual substrate is relaxed by a very dense (average spacing of 5 nm) MD network at the Ge/Si interface. As we demonstrated in a previous work [37], however, contributions coming from MDs can be resolved in strain maps only when their distance is not too small compared with the thickness of the layer. Moreover, in Ref. [36] we characterized the quality of a 2.3 μm-thick Ge layer grown with the same growth recipe of the present one, reporting a TDD in the order of 10^6 cm^{-2} and a RMS roughness around 0.4 nm with micron-scale features. This leads to an average of just 1 TD in the pedestal region and to deviations from the ideal flat top surface of the virtual substrate with negligible aspect ratio. We can thus exclude any effect propagating from the virtual substrate to have significant influence on the strain maps observed in the top $Ge_{1-x}Sn_x$ layer.
As seen in the experimental maps of **Figure 2**, all the components of strain are affected by the presence of the MD network. Yet, the contribution differs for each component, which can be explained by the distortion that dislocations introduce into the lattice. The strain fields induced by MDs close to a crystal surface have been described by analytical equations [30]. These equations can be used to model strain modulations in the center region of the microdisk, where the pedestal is located. However, the footprint of the CHP in the symmetric strain components ε_{xx}, ε_{yy}, ε_{zz} observed at the rim of the microdisk cannot be directly related to the strain field associated to the MDs at the hetero-interface, since the Ge virtual substrate has been etched away leaving behind a free surface. Instead, there is an additional, indirect contribution of MDs that is connected to alloy fluctuations and remains even after removing the virtual substrate.
In fact, strain and alloy composition are entangled during the $Ge_{1-x}Sn_x$ epitaxial growth. The plastic relaxation of the epitaxial strain increases the incorporation efficiency of Sn into the alloy matrix [31]. Therefore, as the critical thickness for plastic relaxation of the $Ge_{1-x}Sn_x$ is exceeded, strain variations due to forming MDs lead to characteristic modulations of the alloy composition that resembles the CHP [32, 33]. In turn, composition inhomogeneities result in stress and thus an additional contribution to elastic strain [18]. The fact that normal components of elastic strain still exhibit a pronounced CHP on the rim of the microdisk (see maps of ε_{xx}, ε_{yy}, ε_{zz} in **Figure 2a-c**), can only be explained by the latter effect – local stress due to alloy fluctuations that are imprinted into the $Ge_{1-x}Sn_x$ layer.
Strikingly, the SXDM maps of the shear strains ε_{xz}, ε_{yz} and ε_{xy} (**Figure 2g-i**) and the twist w_{xy} (**Figure 2o**) feature a prominent signature of the MD network only on the microdisk center, while it is strongly dampened on the rim. This is particularly clear for the in-plane component ε_{xy}. An explanation is that ε_{xy} is not affected by the compositional variations along the **x** or **y** direction: the transversal lattice displacement due to chemical composition does not change along the lines of the CHP assuming translation symmetry. Only the screw-component of the 60° MDs can give rise to ε_{xy}, such that horizontal and vertical lines appearing in the map of **Figure 2i** are an unambiguous signature of existing MDs. Therefore, the dampening of the CHP on the rim in the ε_{xy} map confirms the removal of the MD network at the $Ge_{1-x}Sn_x$/Ge interface by the etching process [34]. The faint

orthogonal lines that are still apparent on the rim may be attributed to dislocations that have climbed or piled higher into the $Ge_{1-x}Sn_x$.

In order to support these results, we performed complementary Scanning TEM (STEM) measurements in cross-section of a ≈ 50 nm-thick lamella, cut by focused ion beam preparation from a microdisk. In the STEM image in **Figure 3a**, the bending of the rim of the microdisk is easily seen. Moreover, the sidewalls of the Ge pillar are curved, which is attributed to an anisotropic etching rate during fabrication.

At the bottom of the pillar, a dense MD network accommodates the plastic relaxation of the 4.2 % lattice mismatch between Si and Ge [35]. Some threading arms are seen to propagate upwards in the STEM image, but their density decays rapidly with increasing height [36]. Nonetheless, we observe modulations of lattice strain in SXDM maps of the Ge pillar (see Supplementary Figure 9), which we attribute to the MD networks at the Ge/Si and $Ge_{1-x}Sn_x$/Ge interfaces.

Figure 3b shows a magnified image of the $Ge_{1-x}Sn_x$/Ge interface, where a second MD network formed with a line density of $\approx 65\ \mu m^{-1}$, highlighted by the cyan arrow. These MDs are generated prior to the structuring of the microdisk, since a partial plastic relaxation of the ≈ 1.8 % lattice mismatch between the growing $Ge_{1-x}Sn_x$ layer and the Ge virtual substrate occurs during the epitaxy process.

Remarkably, germanium, and hence the MD network, have been fully etched below the rim part of the microdisk. However, there are a few additional dislocations seen inside the $Ge_{1-x}Sn_x$ at heights $\approx 100-150$ nm above the free bottom surface of the rim, as indicated by the red arrow. These raised MD segments facilitate additional local plastic relaxation, which effectively results in the formation of two differently strained $Ge_{1-x}Sn_x$ layers and is linked to Sn segregation during growth. These misfit segments should also be visible in the SXDM data, however, their line density of $\approx 4\ \mu m^{-1}$ is much lower compared to those at the $Ge_{1-x}Sn_x$/Ge interface and so their effect on the strain modulations is weak.

This structural insight from the STEM images is corroborated by a depth profile of the Sn content presented in **Figure 3c**, obtained by Energy Dispersive X-ray (EDX) spectroscopy of the Sn emission from a lamella. There, we can observe a separation of the $Ge_{1-x}Sn_x$ material into a ≈ 160 nm-thick lower layer with nearly constant Sn content of $x_{Sn} \approx 10.5$ % and a ≈ 260 nm-thick upper layer in which the Sn content is gradually increasing up to $x_{Sn} \approx 12.9$ % at the top of the microdisk.

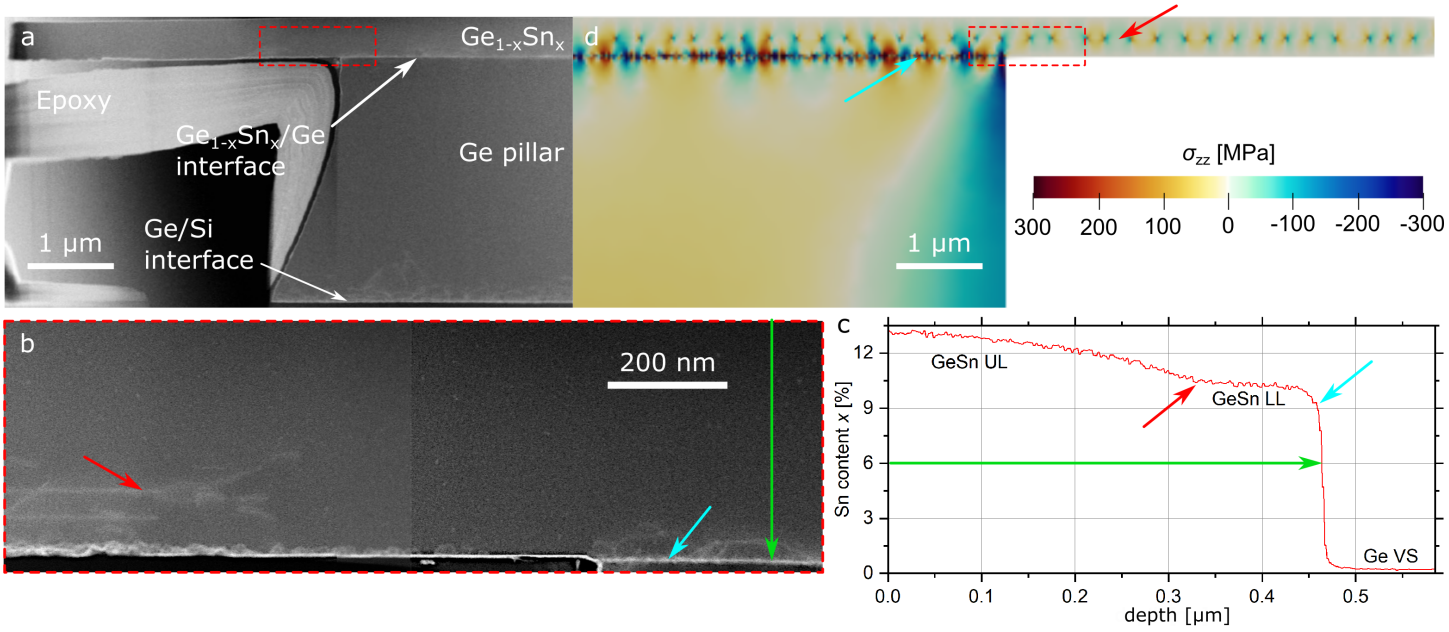

Figure 3: Dislocations, Sn content and surface-normal stress in the microdisk. (a) STEM image in cross section, a high resolution image of the area in the red dashed box is shown in (b). The cyan and red arrows highlight the position of the dense and sparse MD networks, the green arrow indicates the direction to the substrate. (c) EDX depth profile of the Sn content, with lower layer (GeSn LL) and upper layer (GeSn UL). (d) FEM simulation of the surface normal stress σ_{zz} in microdisk and pillar.

The starting point of the composition grading approximately coincides with the depth of the sparse MD network in the STEM images. The strain relief by these MDs facilitates preferential incorporation of the larger Sn atoms.

This leads to the spontaneous generation of a composition grading after the onset of plastic relaxation during epitaxial growth, [29] as is often observed in the literature ([26, 31]). As a result, this microdisk can effectively be considered as a bi-layer system, with upper layer and lower layer having different strain state and alloy composition. We point out that the experimental maps shown in the previous subsection represent a depth average over both $Ge_{1-x}Sn_x$ layers.
The use of FEM models for calculating dislocation-driven displacement fields and the resulting stresses has been demonstrated previously for the description of systems featuring unstructured epitaxial layers [33, 37]. To test our experimental results, we adapted this approach for the microstructure exploiting a 2D FEM model as detailed in the Experimental Section. The average composition was set according to the values obtained from laboratory X-ray diffraction of the unstructured films. Both the dense dislocation network at the interface to the Ge virtual substrate and the sparse MD network inside the $Ge_{1-x}Sn_x$ have been considered in the model, with the Burgers vectors and the positions of the 60° dislocations randomly selected following a log-normal distribution [37, 38] (see Experimental Section for details). The out-of-plane stress σ_{zz} resulting from such simulation for a structure mimicking our microdisk is presented in **Figure 3d**. Only half of the modeled system is reported in the combined image, for comparison with experimental data. Stress fields are emitted from dislocations in the dense MD network at the $Ge_{1-x}Sn_x$/Ge interface (marked by cyan arrow) and the sparse network higher in the microdisk (red arrow). The average MD spacing is $d_{MD} \approx 15$ nm for the former and $d_{MD} \approx 250$ nm for the latter. At the top and bottom free surface of the microdisk, the lattice is free to relax and $\sigma_{zz} = 0$. However, local modulations of σ_{zz} due to the dislocations can be seen within the interior of the microdisk and are especially strong on the supported center part, where the dense MD network is still present. Due to these modulations, the through-film average of σ_{zz} can significantly deviate from zero, which represents a violation of the biaxial stress model typically used for extracting the alloy composition from diffraction data [39]. On the rim of the microdisk, the out-of-plane stress variations are much weaker due to the presence of two free surfaces and a sparser MD density.

2.4 Comparison of layers within the microstructure

As discussed above two $Ge_{1-x}Sn_x$ layers can be distinguished due to changing Sn content and additional plastic relaxation. This is evident in the SXDM signal (see Supplementary Figure 5), featuring two peaks split along the vertical axis of the X-ray detector. The two signals can be analyzed separately, yielding maps of the depth-average strain tensor for each of the two layers. In **Figure 4**, we present experimental maps of the symmetric strain tensor component ε_{zz}, shear strain ε_{yz} and Sn content x_{Sn} for the two $Ge_{1-x}Sn_x$ layers and the Ge pillar. The upper layer (panel **a**) exhibits larger out-of-plane strain ε_{zz} than the lower layer (panel **b**), as the Sn content and thus the lattice mismatch with respect to the Ge pillar increases with height. Moreover, the CHP in the lower layer appears sharper, since it is closer to the MD network in the $Ge_{1-x}Sn_x$/Ge interface resulting in a lower degree of averaging of the MD strain fields (see **Figure 3d**).
The Ge support (panel **c**), is weakly strained in ε_{zz}, due to its dominating thickness. Nevertheless, the imprint of the MD network at the $Ge_{1-x}Sn_x$/Ge interface is clearly seen. Additionally, there is a ring-shaped region of compressive strain along ε_{zz} at the boundary of the pillar, which is likely caused by the pressure exerted from the $Ge_{1-x}Sn_x$ microdisk as it bends downwards at the sides (as also seen in Figure 3d). Another contribution to this compression may be the response of the lattice to a local lateral expansion due to the stress applied by the $Ge_{1-x}Sn_x$ microdisk according to the Poisson effect.

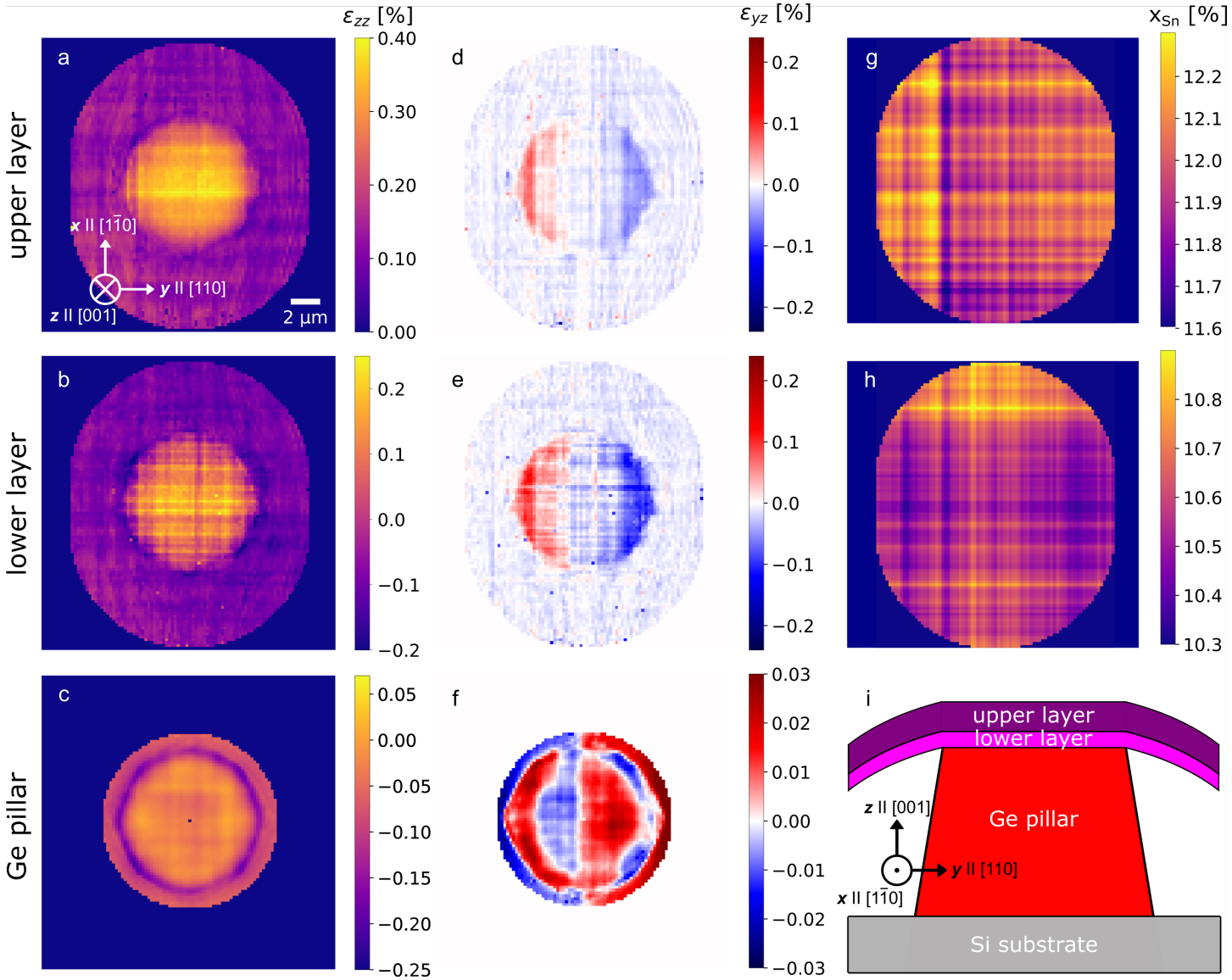

Figure 4: SXDM maps of the upper and lower $Ge_{1-x}Sn_x$ layers and the Ge pillar. (a) - (c) symmetric strain ε_{zz}, (d) - (f) shear strain ε_{yz}, (g) - (h) Sn content x_{Sn}. (l) Schematic of the microdisk in cross section. The inset arrows indicate the lattice directions.

When comparing ε_{yz} in the two $Ge_{1-x}Sn_x$ layers, we notice that the amplitude of the strain dipole in the upper layer (panel **d**) is decreased compared the lower layer (panel **e**) that contains the hetero-interface to the Ge virtual substrate, where the mismatch stress is applied. The same stress is applied to the pillar (panel **f**), but the strain response in ε_{yz} is significantly weaker, since the shear deformation occurs mostly at the topmost region of the pillar, while the SXDM data represent a depth-average over its entire thickness of 2.7 µm. These observations are reproduced by additional FEM simulations, which show that the shear deformation in the Ge pillar is decreasing with the depth (see Supplementary Figure 10).
Maps of the Sn content x_{Sn} are presented in **Figure 4g,h** (the calculation is described in the next subsection). Here, the footprint of the CHP extends over the entire microdisk, since the spatial distribution of Sn content is imprinted during growth by the strain fields from the MD network. This pattern is preserved in the map of x_{Sn} even when after the dislocations themselves are etched away, leaving a "fossil" of the MD network. At later growth stages, the strain fields from MDs in the $Ge_{1-x}Sn_x$/Ge interface superimpose and average out on the growth front. Therefore, the CHP appears on longer spatial length scales in the upper layer (panel **g**) than in the lower layer (panel **h**). As a rule of thumb, the CHP fluctuations of lattice strain and composition take place on a scale corresponding to the distance of the MD network [33].

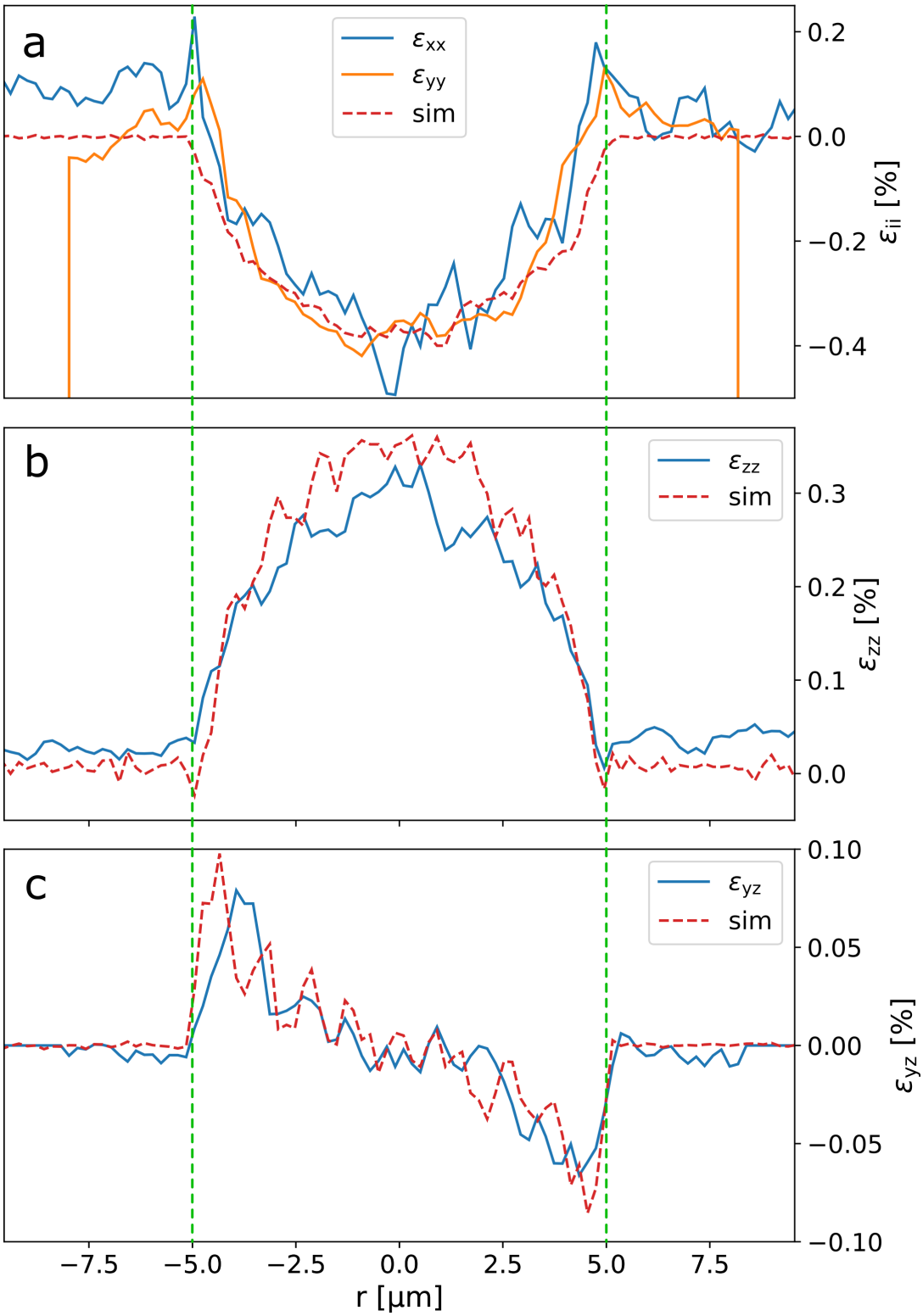

Figure 5: Line profiles of strain tensor components in the microdisk, averaged over the full depth. (a) Experimental profiles of ε_{xx}, ε_{yy} and corresponding FEM simulation (b) Profiles for ε_{zz} and (c) for ε_{yz}. The dashed green lines mark the extent of the supporting Ge pillar.

To allow a quantitative comparison of the simulations and the SXDM experiment, line profiles of different components of the strain tensor are shown in **Figure 5**. The experimental profiles were obtained by taking diametrical line cuts with an integration width of 1 µm across the SXDM maps, considering the average over the two $Ge_{1-x}Sn_x$ layers. The simulated profiles were extracted from the 2D FEM models based on the elastic relaxation and the given MD density, by integration through the thickness of the $Ge_{1-x}Sn_x$ film.
The calculated and measured strain profiles are compared in **Figure 5** and show excellent quantitative agree-

ment. It should be emphasized that the simulation does not aim at reproducing the exact positions of local maxima and minima, since it is based on an randomly-generated position of the MDs (see Experimental Section for details). These modulations affect all components of the strain and are superimposed to the global elastic relaxation. Still, the amplitude of the modulations as well as the overall trends are well reproduced in the simulations. Elastic relaxation of strain is evident as a gradual decrease of the modulus of all normal strain components, ε_{ii} (panels **a, b**), when going from the center (located at $r = 0$) to the free-standing rim of the microdisk. This relaxation converges at the transition region between rim and microdisk center (indicated by the dashed green lines). Interestingly, while the simulation predicts the complete release of lattice strain with $\varepsilon_{xx} \approx \varepsilon_{yy} \approx 0$ on the rim, the experimental profiles show that a small amount of strain of a few 10^{-4} remains in the $Ge_{1-x}Sn_x$. This incomplete relaxation could be related to work hardening due to the dislocations [40], in particular the secondary MD network within the $Ge_{1-x}Sn_x$ unaffected by the under-etching. Alternatively, small structural deviations between the 3D microstructure of the real sample and the ideal device assumed for the simulation could lead to an offset in the strain profile

In contrast, for the shear strain ε_{yz} (panel **c**), elastic relaxation leads to opposite extrema exactly at this transition region, which are connected by a linear gradient, thus resulting in a dipolar distribution.Remarkably, due to the absence of the MD network in the $Ge_{1-x}Sn_x$/Ge interface, the dislocation-driven modulations in the map of shear strain ε_{yz} are strongly attenuated on the rim region in both SXDM data and simulations. On the other hand, the experimental plots of the normal strain components ε_{ii} contain an additional modulation due to lateral fluctuations of the Sn content x_{Sn}, which are not included in the simulations and are discussed in the following.

2.5 Fluctuations of Hydrostatic Strain and Sn content

By default, the change of lattice parameters determined by X-ray diffraction cannot be unambiguously attributed to a particular origin such as changes in stoichiometry, temperature, or local stress. In the study of alloys, a particular challenge is to disentangle the contributions from alloy composition and hydrostatic stress, which both result in an isotropic increase of the unit cell dimensions. Within a thin film, hydrostatic stress equates to the presence of some significant amount of stress σ_{zz} along the surface normal and is usually neglected. However, locally, inhomogeneities and defects in the film can lead to significant values of σ_{zz}. Within our case study on the microdisk, we demonstrate an approach for disentangling these contributions on a sub-micron spatial scale. While the plane-stress approximation ($\sigma_{zz} = 0$) holds true at a free surface, it is not strictly valid within the film [41]. Thus, σ_{zz} may deviate from zero for a SXDM measurement averaged over the probed volume, that is defined by the spot size $\approx 30\,\text{nm} \times 30\,\text{nm}$ and the film thickness (hundreds of nm), thus introducing hydrostatic strain and a potential error for the alloy composition. Within the $Ge_{1-x}Sn_x$ microdisk, we assume the approximation $\sigma_{zz} = 0$ is most appropriate on the free-standing rim, where stress acting along z may be relaxed elastically at both upper and lower free surface. Furthermore, we can expect that the stoichiometry of the $Ge_{1-x}Sn_x$ alloy is not affected by the fabrication of the microdisk.

Thus, the material in the under-etched region should not differ from that in the center region, above the pedestal. Instead, since any spatial modulations of Sn content are due to strain fields from MDs [32], the Sn content map is expected to show only orthogonal lines associated with a regular CHP. Therefore, we parameterize this map by $x_{Sn}(u,v) = \bar{x}_{Sn} + \Delta x^1_{Sn}(u) + \Delta x^2_{Sn}(v)$, where $\bar{x}_{Sn}$ is the average Sn content, Δx^1_{Sn} and Δx^2_{Sn} are the fluctuations and u and v the position coordinates along the directions $\mathbf{x} \parallel [1\bar{1}0]$ and $\mathbf{y} \parallel [110]$.

Figure 6a shows a map of the Sn content x_{Sn} calculated with equations 1 and 3 (see Experimental Section) from the SXDM data by assuming $\sigma_{zz} = 0$ and averaging over the depth of the microdisk. Contrary to the expectation outlined above, the center region can be distinguished from the free-standing rim, which we attribute to a significant deviation of out-of-plane stress σ_{zz} within the center region from zero. This leads to an error on the order of 0.3 % at. in Sn content for 100 MPa of pressure in σ_{zz}.

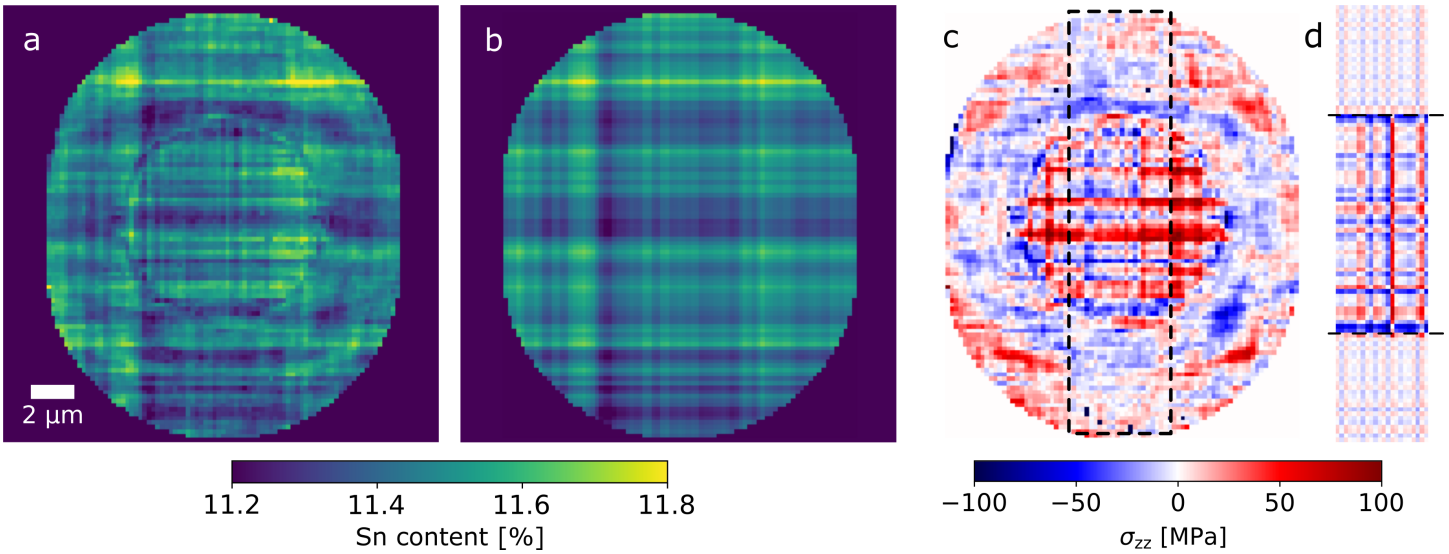

Figure 6: Maps of Sn content x_{Sn} and surface normal stress σ_{zz}. (a) Map of x_{Sn} calculated from Hooke's law assuming $\sigma_{zz} = 0$. (b) Map of x_{Sn} obtained by interpolation of undulations from the rim towards the center. (c) Experimental map of σ_{zz}. (d) Simulation of σ_{zz} in the region marked by the dashed box in (c), the dashed lines indicate the extent of the Ge pillar.

Assuming the fluctuations follow the CHP as described above, a realistic map of the Sn content can be obtained by interpolating the regular undulations in $x_{Sn}(u,v)$ from the rim onto the interior of the microdisk. The result is presented in **Figure 6b**. By re-arranging equation 2, the difference between panels **b** and **a** allows to calculate a map of σ_{zz}, which is presented in **Figure 6c**.
Firstly, we observe a ring of compressive stress around the edge of the Ge pillar, that is attributed to stress applied by the relaxed ring due to the Poisson effect in conjunction with the absence of in-plane strain. With increasing distance from the center, the absolute value of strain ε_{zz} in the $Ge_{1-x}Sn_x$ decays slower than the polar components (e.g. ε_{yy}) owing to the elastic interaction with the strained part on top of the pillar. The corresponding negative elastic stress is visible close to the border of the center region of the microdisk in the maps of σ_{zz}. Moreover, the CHP is seen prominently in the center region of these maps, which can be attributed to σ_{zz} stress fields of MDs in the interface between pillar and microdisk. This pattern fades out on the rim, since the stress from the dislocations can relax elastically at the free bottom surface. These features can be quantitatively reproduced by FEM modeling, shown in **Figure 6d** based on a random distribution of dislocations. The depth average of σ_{zz} has been considered for the two MD networks in the $Ge_{1-x}Sn_x$, for both in-plane directions **x** and **y**. To simplify the calculations, we modeled a rectangular rather than cylindrical structure, taking the free bottom surface on the rim into account. There is an excellent agreement between the simulations and the maps of σ_{zz} calculated from the SXDM data by our approach, which is remarkable considering that the internal stress of a material is typically not accessible by experimental means, especially within a submicron volume.
The spatial modulations of Sn content and lattice strain in the microdisk shift the energy levels of both conduction and valence band, resulting in local fluctuations of the bandgap E_g, which is potentially detrimental to the application as photodiodes or lasers. From calculations of the strain-dependent band energy levels (provided in the SI), we anticipate broadening of the laser emission spectra on the order of 5 meV due to the fluctuations of Sn content and eigenstrain that are still present on the under-etched rim.

3 Conclusion

In this work, we have achieved a thorough description of the 3D lattice strain and composition fluctuation in a multilayered, deformed $Ge_{1-x}Sn_x/Ge$ microdisk thanks to 5D diffraction data that allows to partition the sample both in real and reciprocal space. In a broader sense, we show how multidimensional diffraction data reveal the larger picture of structural heterogeneity. Using this approach, we obtained nanoscale maps for each component of the rotation and strain tensors, allowing deep insights into the mechanisms of elastic and plastic relaxation by separating the contributions of geometric constraints, lattice defects, and alloy stoichiometry.

Remarkably, we observed that, while the network of MDs present at the $Ge_{1-x}Sn_x/Ge$ heterointerface has been removed at the suspended disk periphery during the microfabrication process, a "fossilized" footprint of these structural defects remains in the layer in the form of spatial strain modulation. The latter is induced by a local modulation of the Sn content, which in turn is generated by the formation of the MD network during epitaxy. In addition, we were able to obtain a "tomographic" view of the sample. By separating the signals of individual layers in reciprocal space, we observed how the footprint of the MD network propagates across sublayers parallel to the sample surface that differ in Sn content.
The experimental results are corroborated by theoretical calculations based on advanced mechanical models that closely mimic the real microstructure, taking into account both plastic relaxation from dislocation formation and elastic interaction arising from 3D patterning. We find excellent agreement between experiment and theory for all components of the strain tensor, including the shear strains, which are usually difficult to resolve.
As a model system, the microdisk offers unique insight into relaxation mechanisms caused by micro-patterning. Thus, by comparison of the free-standing rim of the disk with its center region that is connected to the Ge pillar, we were able to estimate hydrostatic stress contributions from the diffraction data and, hence, to test the typical assumptions that are made in the determination of alloy composition. In particular, near dislocations or pattern edges, we find significant values of the through-film average of surface normal stress σ_{zz} in the alloyed epitaxial layer, which are in good agreement to the presented FEM calculations. Contrary to what is commonly reported in literature, this contribution cannot be considered negligible when calculating the alloy composition.
We believe that the level of quantification enabled by scanning X-ray diffraction microscopy, as demonstrated in this work, has great potential to improve our understanding of 3D microstructures, particularly in the presence of anisotropic deformation. The unique strain sensitivity and spatial resolution of the SDXM technique goes beyond that of established methods, in particular for the shear components. Since the sample remains intact throughout the measurement, it is suitable for correlative studies with other techniques probing microscopic fluctuations of sample properties. Because SXDM is model-free, non-destructive, and capable of analyzing any crystalline sample, it has the potential to be applied to a wide range of problems in diverse disciplines such as semiconductor technology, mechanical testing, metallurgy, and biophysics.

4 Experimental Section

Materials:
The sample consists of a $Ge_{1-x}Sn_x$ microdisk on a Ge pillar, fabricated by selective dry-etching from epitaxial layers deposited by Chemical Vapor Deposition on commercial Si(001) substrates. The Ge pillar is 2.7 µm thick with a diameter of $\approx 10\ \mu$m and the $Ge_{1-x}Sn_x$ microdisk is 420 nm thick with diameter ≈ 20 µm.

SXDM Measurements:
The experiments were performed at the hard X-ray nanoprobe beamline ID01/ESRF [42], where they benefit from the recent Extremely Bright Source (EBS) upgrade to the storage ring, making ESRF the brightest synchrotron source to-date [43]. The small emittance of the source and high brilliance of the beam is optimal for the study of thin epitaxial layers [17].
The X-ray energy was set to 9.5 keV and the beam is focused to a diameter of ≈ 30 nm diameter on the sample surface by a Fresnel Zone Plate (FZP), while the higher order diffraction is blocked by an Order Sorting Aperture (OSA). The characteristics of the beam focused with this FZP are described in the Supporting Information of Ref. [25]. The Bragg condition of the $\{335\}$ reflection of $Ge_{1-x}Sn_x$ is met at an incidence angle of $\approx 90°$, avoiding any significant broadening of the beam footprint by projection on the sample surface.
Mapping was achieved by scanning the sample across the X-ray beam with a piezo stage while continuously reading out the diffraction signal on an X-ray area detector. Due to the high brilliance, an exposure time of 10 ms per spot on the sample is sufficient to measure the signal from the $Ge_{1-x}Sn_x$ layer. These diffraction maps are measured for a series of rocking angles ω to sample the 3D reciprocal space around the $\{335\}$ Bragg reflections [18]. A particular experimental challenge is the strong bending of the microdisks that is a consequence of local elastic relaxation. Because of the strong bending on the rim, a large range $> 5\,°$ in ω was scanned to cover the reflection across the microdisk. Moreover, the $Ge_{1-x}Sn_x$ Bragg peak also moves along the horizontal axis of

the detector due to any bending perpendicular to the scattering plane. This is particulary prominent on the edges of the rim along $y \parallel [110]$ and leads to the signal moving off the area detector during the raster scan, which is the cause of the missing regions in the experimental data in Figure 2.
Since a single scattering vector is insufficient to calculate the nine independent components of rotation and strain, SXDM measurements were performed for three different non-coplanar Bragg reflections (335, $3\bar{3}5$ and $\bar{3}\bar{3}5$). A linear combination of the three scattering vectors allows to calculate the lattice parameters and the strain according to the equations provided in Ref. [25].
Figure 7 illustrates the effect of the symmetric strain tensor components on the $Ge_{1-x}Sn_x$ unit cell, changing the cubic lattice parameters $a = b = c$ to $a' \neq b' \neq c'$. Panel **a** shows a cubic unit cell, which corresponds to an unstrained lattice and approximately describes the $Ge_{1-x}Sn_x$ lattice on the strain-relaxed rim of the microdisk. In panel **b**, a highly deformed unit cell is shown, corresponding to the $Ge_{1-x}Sn_x$ lattice in the strained center of the microdisk.

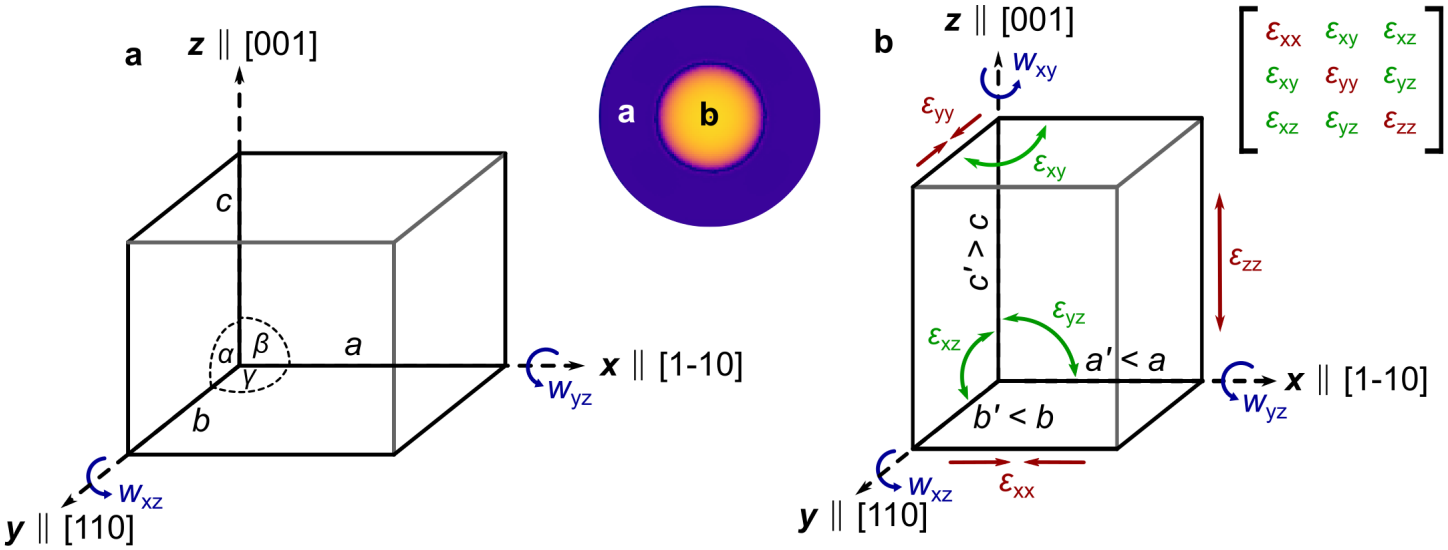

Figure 7: Strain tensor components in a cubic lattice. (a) Unstrained and (b) highly strained unit cell. The insets show the simulated map of ε_{zz} and the strain tensor in matrix form.

Calculation of local Sn content:
The unstrained lattice parameter a_0 for the $Ge_{1-x}Sn_x$ alloy, which describes the dimensions of its cubic unit cell ($a_0 = a = b = c$) is related to the Sn content according to equation 1, which is determined empirically in Ref. [44].

$$a_0 = a_{Ge}(1 - x_{Sn}) + a_{Sn}x_{Sn} + f_{bow}x_{Sn}(1 - x_{Sn}) \tag{1}$$

Here, $a_{Ge} = 0.5658$ nm and $a_{Sn} = 0.6489$ nm are the lattice parameters of Ge and α-Sn [45], and $f_{bow} = 0.0041$ nm is the bowing parameter that describes the deviation of the function $a_0(x_{Sn})$ from the linear Vegard's law for $Ge_{1-x}Sn_x$.
With equation 1, the Sn content x_{Sn} is linked to the unstrained parameter a_0, which can be calculated locally from SXDM: By rearranging Hooke's law for the surface normal component σ_{zz}, we obtain equation 2, linking a_0 to the parameters a, b, c of the strained lattice determined experimentally from the SXDM dataset:

$$a_0 = \frac{C_{13}(a+b) + C_{33}c}{\sigma_{zz} + 2C_{13} + C_{33}} \tag{2}$$

$C_{13} = C_{23}$ and C_{33} are components of the 6×6 elasticity tensor in $Ge_{1-x}Sn_x$, which are typically assumed by linear interpolation between the values for Ge and α-Sn.
Solving equation 2 requires knowledge of σ_{zz}, which is difficult to access experimentally. A common approach to overcome this limitation in the case of thin films is the plane-stress approximation assuming $\sigma_{zz} = 0$, which is

equivalent to a biaxial stress state with ε_{zz} being driven exclusively by the Poisson effect. Assuming $\sigma_{zz} = 0$, this yields the often-used equation 3 with the Poisson number $\nu_{13} \approx \nu_{23}$ [39].

$$a_0 = \frac{\nu_{13}(a+b) + (1-\nu_{13})c}{1+\nu_{13}} \tag{3}$$

Lamella fabrication and TEM measurements:
The lamellas were extracted in cross-section from the $Ge_{1-x}Sn_x$/Ge microdisk by Focused Ion Beam (FIB) with a *Helios 5 UC* system. The sample surface was covered by a protective carbon layer to prevent amorphization of the surface and a epoxy filling was applied to support the free-standing rim of the microdisk. The STEM measurements were performed with an aberration-corrected *JEOL ARM200F* TEM system.

FEM Simulation of elastic relaxation:
Simulations of the elastic relaxation of the microdisk on the rim and the resulting strain were performed with *Comsol Multiphysics* exploiting the Solid Mechanics module, assuming the linear elastic theory. The input parameters for the FEM model, which is described in detail in Ref. [46], were the geometry of the microdisks, as known from SEM images, the spatially averaged Sn content and strain state of each layer, as obtained from laboratory XRD measurements and the Young's modulus and Poisson numbers of $Ge_{1-x}Sn_x$ and Ge assumed from the literature [47].

Dislocation Simulations:
We simulated SXDM data exploiting a continuum approach based on the linear elastic theory. The dislocation fields (strain and rotational) have been calculated by solving the Partial Differential Equation (PDE) of mechanical equilibrium by means of the FEM [11]. The dislocations are modeled by exploiting the eigenstrain method [48]. The eigenstrain tensor is calculated by exploiting the strain field expressions of dislocations in an infinite media (see Ref. [49]). The boundary conditions of the PDE are then applied according to the system under consideration. The bottom of the pillar is kept fixed (Dirichlet Boundary condition) while all the other external boundaries are free surfaces (zero normal stress or Neumann boundary condition). By solving the mechanical equilibrium PDE by means of the FEM we are thus able to obtain the exact solution of the dislocations fields inside the heterostructure, consistently with the boundary conditions. The heteroepitaxial strain field was also modeled by means of the eigenstrain approach by initializing a biaxial strain tensor consistent with the average Sn content in the $Ge_{1-x}Sn_x$ layers obtained by XRD. For the microdisk, the 420-nm thick heterolayer has been modeled by two separate $Ge_{1-x}Sn_x$ layers with slightly different Sn content: the bottom layer is 260 nm-thick and has an average Sn content of 10.8%, the upper one is 160 nm-thick and has an average Sn content of 11.8%.
The nearest-neighbour distribution of the MDs has been reproduced by a log-normal distribution, as demonstrated several times for different systems [37, 33, 38, 50]. The distribution:

$$f(r) = \frac{1}{r\sqrt{2\pi}\alpha} \exp -\frac{(\ln r - \mu)^2}{2\alpha^2} \tag{4}$$

is parametrized by two parameters: μ, representing the logarithm of the average distance between adjacent dislocations and α the dispersion of the distribution. This distribution was used to define the MD network with the parameter μ being adjusted based on the average Sn composition and the observed degree of relaxation. The orientation of the individual Burgers vectors was randomly assigned, again following the results of Ref. [37].

Supporting information Supporting Information is available from the Wiley Online Library or from the author.

Acknowledgements We acknowledge the European Synchrotron Radiation Facility (ESRF) for provision of synchrotron radiation facilities and we would like to thank the staff for assistance in using beamline ID01. Furthermore, the authors acknowledge support from IKZ staff regarding EDX measurements (Dr. T. Schulz), electron channeling contrast imaging (C.-H. Lu), and proofreading (Dr. M. Schmidbauer).

Data availability The datasets generated during and/or analysed during the current study are available in the ESRF data repository (https://doi.esrf.fr/10.15151/ESRF-ES-514136653). Derived data are available from the corresponding author on reasonable request.

Conflicts of Interest The authors declare no conflicts of interest.

References

[1] S. Dolabella, A. Borzì, A. Dommann, A. Neels, *Small Methods* **2022**, *6*, 2 2100932.

[2] Y. Guo, Z. Xu, A. G. Curto, Y.-J. Zeng, D. Van Thourhout, *Progress in Materials Science* **2023**, 101158.

[3] W. Chen, X. Zhan, R. Yuan, S. Pidaparthy, A. X. B. Yong, H. An, Z. Tang, K. Yin, A. Patra, H. Jeong, C. Zhang, K. Ta, Z. W. Riedel, R. M. Stephens, D. P. Shoemaker, H. Yang, A. A. Gewirth, P. V. Braun, E. Ertekin, J.-M. Zuo, Q. Chen, *Nature Materials* **2023**, *22*, 1 92.

[4] B. Liu, J. Li, G. Wang, F. Ye, H. Yan, M. Zhang, S.-C. Dong, L. Lu, P. Huang, T. He, P. Xu, H.-S. Kwok, G. Li, *Science Advances* **2022**, *8*, 38.

[5] V. Karthikeyan, J. U. Surjadi, X. Li, R. Fan, V. C. Theja, W. J. Li, Y. Lu, V. A. Roy, *Nature Communications* **2023**, *14*, 1 2069.

[6] C. Atlan, C. Chatelier, I. Martens, M. Dupraz, A. Viola, N. Li, L. Gao, S. J. Leake, T. U. Schülli, J. Eymery, F. Maillard, M.-I. Richard, *Nature Materials* **2023**, 1–8.

[7] R. J. Hickey, M. Leblanc Latour, J. L. Harden, A. E. Pelling, *Advanced Engineering Materials* **2023**, 2201415.

[8] G. Scappucci, C. Kloeffel, F. A. Zwanenburg, D. Loss, M. Myronov, J.-J. Zhang, S. De Franceschi, G. Katsaros, M. Veldhorst, *Nature Reviews Materials* **2021**, *6*, 10 926.

[9] J. Chretien, N. Pauc, F. Armand Pilon, M. Bertrand, Q.-M. Thai, L. Casiez, N. Bernier, H. Dansas, P. Gergaud, E. Delamadeleine, R. Khazaka, H. Sigg, J. Faist, A. Chelnokov, V. Reboud, J.-M. Hartmann, V. Calvo, *ACS Photonics* **2019**, *6*, 10 2462.

[10] J. Chrétien, Q. Thai, M. Frauenrath, L. Casiez, A. Chelnokov, V. Reboud, J. Hartmann, M. El Kurdi, N. Pauc, V. Calvo, *Applied Physics Letters* **2022**, *120*, 5 051107.

[11] F. Rovaris, F. Isa, R. Gatti, A. Jung, G. Isella, F. Montalenti, H. von Känel, *Physical Review Materials* **2017**, *1*, 7 073602.

[12] K. Shida, S. Takeuchi, Y. Imai, S. Kimura, A. Schulze, M. Caymax, A. Sakai, *ACS Applied Materials & Interfaces* **2017**, *9*, 15 13726.

[13] Q. Chen, L. Zhang, Y. Song, X. Chen, S. Koelling, Z. Zhang, Y. Li, P. M. Koenraad, J. Shao, C. S. Tan, S. Wang, Q. Gong, *ACS Applied Nano Materials* **2021**, *4*, 1 897.

[14] A. Bashir, R. W. Millar, K. Gallacher, D. J. Paul, A. D. Darbal, R. Stroud, A. Ballabio, J. Frigerio, G. Isella, I. MacLaren, *Journal of Applied Physics* **2019**, *126*, 23.

[15] H. Yu, J. Liu, P. Karamched, A. J. Wilkinson, F. Hofmann, *Scripta Materialia* **2019**, *164* 36.

[16] T. E. Edwards, X. Maeder, J. Ast, L. Berger, J. Michler, *Science Advances* **2022**, *8*, 30 5735.

[17] T. U. Schülli, S. J. Leake, *Current Opinion in Solid State and Materials Science* **2018**, *22*, 5 188.

[18] C. Richter, V. M. Kaganer, A. Even, A. Dussaigne, P. Ferret, F. Barbier, Y.-M. Le Vaillant, T. U. Schülli, *Physical Review Applied* **2022**, *18*, 6 064015.

[19] M. Gonzalez-Zalba, S. De Franceschi, E. Charbon, T. Meunier, M. Vinet, A. Dzurak, *Nature Electronics* **2021**, *4*, 12 872.

[20] S. B. Samavedam, J. Ryckaert, E. Beyne, K. Ronse, N. Horiguchi, Z. Tokei, I. Radu, M. G. Bardon, M. H. Na, A. Spessot, S. Biesemans, In *2020 IEEE International Electron Devices Meeting (IEDM)*. **2020** 1.1.1–1.1.10.

[21] P. Chaisakul, D. Marris-Morini, J. Frigerio, D. Chrastina, M.-S. Rouifed, S. Cecchi, P. Crozat, G. Isella, L. Vivien, *Nature Photonics* **2014**, *8*, 6 482.

[22] M. M. Waldrop, *Nature News* **2016**, *530*, 7589 144.

[23] D. Buca, A. Bjelajac, D. Spirito, O. Concepción, M. Gromovyi, E. Sakat, X. Lafosse, L. Ferlazzo, N. von den Driesch, Z. Ikonic, D. Grützmacher, G. Capellini, M. El Kurdi, *Advanced Optical Materials* **2022**, 2201024.

[24] B. Marzban, L. Seidel, T. Liu, K. Wu, V. Kiyek, M. H. Zoellner, Z. Ikonic, J. Schulze, D. Gruetzmacher, G. Capellini, M. Oehme, J. Witzens, D. Buca, *ACS Photonics* **2022**, *10*, 1 217.

[25] C. Corley-Wiciak, C. Richter, M. H. Zoellner, I. Zaitsev, C. L. Manganelli, E. Zatterin, T. U. Schuelli, A. A. Corley-Wiciak, J. Katzer, F. Reichmann, W. M. Klesse, N. W. Hendrickx, A. Sammak, M. Veldhorst, G. Scappucci, M. Virgilio, G. Capellini, *ACS Applied Materials & Interfaces* **2023**.

[26] H. Stanchu, A. V. Kuchuk, Y. I. Mazur, J. Margetis, J. Tolle, J. Richter, S.-Q. Yu, G. J. Salamo, *Semiconductor Science and Technology* **2020**, *35*, 7 075009.

[27] J. Bharathan, J. Narayan, G. Rozgonyi, G. E. Bulman, *Journal of electronic materials* **2013**, *42* 40.

[28] R. Beanland, D. Dunstan, P. Goodhew, *Advances in Physics* **1996**, *45*, 2 87.

[29] W. Dou, M. Benamara, A. Mosleh, J. Margetis, P. Grant, Y. Zhou, S. Al-Kabi, W. Du, J. Tolle, B. Li, M. Mortazavi, S.-Q. Yu, *Scientific reports* **2018**, *8*, 1 5640.

[30] V. M. Kaganer, R. Köhler, M. Schmidbauer, R. Opitz, B. Jenichen, *Physical Review B* **1997**, *55*, 3 1793.

[31] H. V. Stanchu, A. V. Kuchuk, Y. I. Mazur, J. Margetis, J. Tolle, S.-Q. Yu, G. J. Salamo, *Applied Physics Letters* **2020**, *116*, 23.

[32] M. H. Zoellner, M.-I. Richard, G. A. Chahine, P. Zaumseil, C. Reich, G. Capellini, F. Montalenti, A. Marzegalli, Y.-H. Xie, T. U. Schulli, M. Häberlen, P. Storck, T. Schroeder, *ACS applied materials & interfaces* **2015**, *7*, 17 9031.

[33] F. Rovaris, M. H. Zoellner, P. Zaumseil, A. Marzegalli, L. Di Gaspare, M. De Seta, T. Schroeder, P. Storck, G. Schwalb, G. Capellini, F. Montalenti, *Phys. Rev. B* **2019**, *100* 085307.

[34] A. Elbaz, R. Arefin, E. Sakat, B. Wang, E. Herth, G. Patriarche, A. Foti, R. Ossikovski, S. Sauvage, X. Checoury, K. Pantzas, I. Sagnes, J. Chretien, L. Casiez, M. Bertrand, V. Calvo, N. Pauc, A. Chelnokov, P. Boucaud, F. Boeuf, V. Reboud, J.-M. Hartmann, M. El Kurdi, *ACS photonics* **2020**, *7*, 10 2713.

[35] J. P. Dismukes, L. Ekstrom, R. J. Pfaff, *J. Phys. Chem.* **1964**, *68* 3021.

[36] O. Skibitzki, M. H. Zoellner, F. Rovaris, M. A. Schubert, Y. Yamamoto, L. Persichetti, L. Di Gaspare, M. De Seta, R. Gatti, F. Montalenti, et al., *Physical Review Materials* **2020**, *4*, 10 103403.

[37] F. Rovaris, M. H. Zoellner, P. Zaumseil, M. A. Schubert, M. A., L. Di Gaspare, M. De Seta, T. Schroeder, P. Storck, G. Schwalb, C. Richter, T. U. Schülli, G. Capellini, F. Montalenti, *Physical Review Applied* **2018**, *10*, 054067.

[38] K. K. Sabelfeld, V. M. Kaganer, C. Pfüller, O. Brandt, *Journal of Physics D: Applied Physics* **2017**, *50*, 40 405101.

[39] J. J. Wortman, R. A. Evans, *J. Appl. Phys.* **1965**, *36* 153.

[40] G. Capellini, M. De Seta, P. Zaumseil, G. Kozlowski, T. Schroeder, *Journal of Applied Physics* **2012**, *111*, 7.

[41] C. Corley-Wiciak, M. Zoellner, I. Zaitsev, K. Anand, E. Zatterin, Y. Yamamoto, A. Corley-Wiciak, F. Reichmann, W. Langheinrich, L. Schreiber, C. Manganelli, M. Virgilio, C. Richter, G. Capellini, *Phys. Rev. Appl.* **2023**, *20* 024056.

[42] S. J. Leake, G. A. Chahine, H. Djazouli, T. Zhou, C. Richter, J. Hilhorst, L. Petit, M.-I. Richard, C. Morawe, R. Barrett, L. Zhang, R. A. Homs-Regojo, V. Favre-Nicolin, P. Boesecke, T. U. Schulli, *Journal of synchrotron radiation* **2019**, *26*, 2 571.

[43] P. Raimondi, C. Benabderrahmane, P. Berkvens, J. C. Biasci, P. Borowiec, J.-F. Bouteille, T. Brochard, N. B. Brookes, N. Carmignani, L. R. Carver, et al., *Communications Physics* **2023**, *6*, 1 82.

[44] F. Gencarelli, B. Vincent, J. Demeulemeester, A. Vantomme, A. Moussa, A. Franquet, A. Kumar, H. Bender, J. Meersschaut, W. Vandervorst, R. Loo, M. Caymax, K. Temst, M. Heyns, *ECS Journal of Solid State Science and Technology* **2013**, *2*, 4 P134.

[45] M. Oehme, J. Werner, M. Gollhofer, M. Schmid, M. Kaschel, E. Kasper, J. Schulze, *IEEE Photonics Technology Letters* **2011**, *23*, 23 1751.

[46] I. Zaitsev, A. A. Corley-Wiciak, C. Corley-Wiciak, M. H. Zoellner, C. Richter, E. Zatterin, M. Virgilio, B. Martín-García, D. Spirito, C. L. Manganelli, *physica status solidi (RRL)–Rapid Research Letters* **2023**, 2300348.

[47] P. Lytvyn, A. Kuchuk, S. Kondratenko, H. Stanchu, S. V. Malyuta, S.-Q. Yu, Y. I. Mazur, G. J. Salamo, *Applied Physics Letters* **2023**, *123*, 2.

[48] T. Mura, *Micromechanics of defects in solids*, Springer Science & Business Media, **2013**.

[49] P. M. Anderson, J. P. Hirth, J. Lothe, *Theory of dislocations*, Cambridge University Press, **2017**.

[50] L. Becker, P. Storck, T. Schulz, M. H. Zoellner, L. Di Gaspare, F. Rovaris, A. Marzegalli, F. Montalenti, M. De Seta, G. Capellini, G. Schwalb, T. Schroeder, M. Albrecht, *Journal of Applied Physics* **2020**, *128*, 21.

Table of Contents

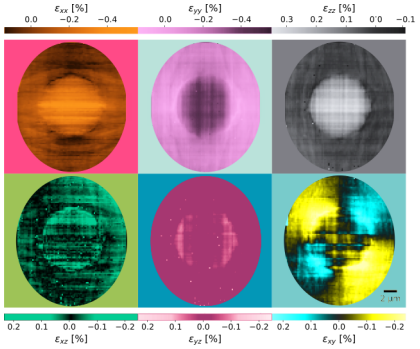

The deformation landscape of a strongly bent $Ge_{1-x}Sn_x$ microdisk for CMOS-compatible optoelectronics is quantified by Scanning X-ray Diffraction Microscopy, a synchrotron-based nanoprobe technique with < 100 nm spatial resolution and fine lattice sensitivity $< 10^{-4}$. This study demonstrates how the detailed analysis of multi-dimensional diffraction data enables complete disentanglement of strain, stress, rotation and stoichiometry within complex, three-dimensional microstructures.